

Detection of Complex Organic Molecules in Young Starless Core L1521E

Samantha Scibelli,¹* Yancy Shirley,¹ Anton Vasyunin² and Ralf Launhardt³

¹*Steward Observatory, University of Arizona, Tucson, AZ 85721*

²*Ural Federal University, Ekaterinburg, Russia*

³*Max-Planck-Institut für Astronomie Königstuhl 17, D9117 Heidelberg, Germany*

Accepted XXX. Received YYY; in original form ZZZ

ABSTRACT

Determining the level of chemical complexity within dense starless and gravitationally bound prestellar cores is crucial for constructing chemical models, which subsequently constrain the initial chemical conditions of star formation. We have searched for complex organic molecules (COMs) in the young starless core L1521E, and report the first clear detection of dimethyl ether (CH_3OCH_3), methyl formate (HCOOCH_3), and vinyl cyanide (CH_2CHCN). Eight transitions of acetaldehyde (CH_3CHO) were also detected, five of which (A states) were used to determine an excitation temperature to then calculate column densities for the other oxygen-bearing COMs. If source size was not taken into account (i.e., if filling fraction was assumed to be one), column density was underestimated, and thus we stress the need for higher resolution mapping data. We calculated L1521E COM abundances and compared them to other stages of low-mass star formation, also finding similarities to other starless/prestellar cores, suggesting related chemical evolution. The scenario that assumes formation of COMs in gas-phase reactions between precursors formed on grains and then ejected to the cold gas via reactive desorption was tested and was unable to reproduce observed COM abundances, with the exception of CH_3CHO . These results suggest that COMs observed in cold gas are formed not by gas-phase reactions alone, but also through surface reactions on interstellar grains. Our observations present a new, unique challenge for existing theoretical astrochemical models.

Key words: astrochemistry – submillimetre: ISM – radiative transfer

1 INTRODUCTION

The chemistry of star and planet formation begins with the synthesis of molecules in interstellar molecular clouds. Dense ($\sim 10^5 \text{ cm}^{-3}$) and cold (10 K) regions within these clouds, called starless and gravitationally bound prestellar cores, represent the earliest observable stage of low-mass ($M \leq \text{few } M_\odot$) star-formation (di Francesco et al. 2007; Bergin & Tafalla 2007; André et al. 2014). It is during this phase prior to the formation of a first hydrostatic core (the foremost stage of a protostar), that the initial conditions for star and planet formation are set.

In the warm regions of early star formation, such as in hot cores and hot corinos, rich chemistry has been explained by a warm-up, gas-phase chemistry driven by the heat from the forming protostar that sublimates ice mantles (Jørgensen et al. (2020) and references therein). Surprisingly, even in cold and shielded environments, rotational transitions of complex organic molecules (COMs) have been detected in the gas phase toward dense prestellar cores from deep millimeter wave observations (Öberg et al. 2010; Bacmann et al. 2012; Jiménez-Serra et al. 2016; Scibelli & Shirley 2020). These large (≥ 6 atom) carbon-bearing molecules are of astrobiological significance, and their presence prior to protostar and planet formation provides insight into COM formation histories.

There is still, however, a significant gap in our understanding of

the development of COMs during this initial phase of low-mass star formation. The traditional picture depicts COMs forming in CO and H_2O rich ices that are irradiated by UV light and cosmic rays (Watanabe & Kouchi 2002; Chuang et al. 2017). The subsequent formation of radicals in the warming ice, during the development of a hot corino, leads to the formation of complex organic species that are released into the gas phase when the young, accreting protostar heats up the dust grains above the sublimation temperature of the ices (Garrod & Herbst 2006; Aikawa et al. 2008; Herbst & van Dishoeck 2009). Since prestellar cores have no internal heating source, several different scenarios of cold COMs formation have been proposed, including the desorption of radicals, yet their relative importance is not currently clear.

If COMs form in the ices, then the subsequent desorption of COMs in the outer, icy layers of prestellar cores appears to occur at a rate fast enough to build up an observable abundance of COMs (Vastel et al. 2014). Alternatively, COMs could form in the gas phase through neutral-neutral reactions from the chemical desorption of radicals formed in the ice (Vasyunin & Herbst 2013; Vasyunin et al. 2017). New non-diffusive chemical models produce excited radicals instead by surface or bulk reactions, which leads to an enhancement of COM abundance in cold core conditions (Jin & Garrod 2020). In order to discern between different formation scenarios, we must understand the physical conditions in which COMs form as well as constrain their abundances.

The discovery of COMs in prestellar cores leads to fundamental

*E-mail: sscibelli@email.arizona.edu

questions of how quickly these COMs form, and to what level of complexity. In our previous study of a large sample (31) of starless and prestellar cores within the Taurus Molecular Cloud (Scibelli & Shirley 2020), we found a prevalence of the ‘mother molecule,’ methanol (CH_3OH ; 100% detection rate), which is the gas precursor of several COMs, as well as acetaldehyde (CH_3CHO ; 70% detection rate). For the larger molecules, like dimethyl ether (CH_3OCH_3) and methyl formate (HCOOCH_3), surveys have been limited to a few well-studied, evolved and dense objects, i.e., L1689B in Ophiuchus (Bacmann et al. 2012) and L1544 in Taurus (Jiménez-Serra et al. 2016). L1544 is the densest known prestellar core, with well developed collapse motions and a central density $> 10^7 \text{cm}^{-3}$ (Caselli et al. 2019). Species such as CH_3O , CH_3CHO and CH_3OCH_3 are enhanced in L1544 by factors of $\sim 2 - 10$ toward the CH_3OH peak with respect to (w.r.t.) the core’s center (Jiménez-Serra et al. 2016). It has been suggested that HCOOCH_3 and CH_3OCH_3 are synthesised in gas-phase reactions with CH_3OH and other precursor species ejected from grains via the process of reactive desorption (Vasyunin et al. 2017). We know that CH_3OH and CH_3CHO are prevalent in the starless and prestellar cores in Taurus (Scibelli & Shirley 2020), now we look for more complex species.

In this study we targeted a dynamically and chemically young starless core in Taurus, Lynds 1521E (L1521E). It has a modest central density of $2 - 3 \times 10^5 \text{cm}^{-3}$, no kinematic evidence for collapse, little evidence for freezeout of CO (\lesssim factor of 2), and little evidence for chemically evolved indicators, such as abundant deuterated molecules (Tafalla & Santiago 2004; Ford & Shirley 2011). L1521E can only have existed at its present density of $> 10^5 \text{cm}^{-3}$ for less than 10^5 years, otherwise there would be more significant CO freezeout (e.g., see Redman et al. (2002)). Uniquely, L1521E is also one of only two cores known in Taurus, the other Seo 32 in the B213 region, where the ‘early-time’ chemical tracers (such as CCS and HC_3N) peak strongly at the same position as the dust continuum peak (Suzuki et al. 1992; Seo et al. 2019). Furthermore, ‘late-time’ chemical tracers such as NH_3 , N_2H^+ , and deuterated species are very weak (Hirota et al. 2001; Nagy et al. 2019). The chemical and kinematical evidence agree that this object is one of the youngest starless cores known, with densities at $> 10^5 \text{cm}^{-3}$. Thus, L1521E is an excellent object toward which to test the limits of how quickly COMs form, to test what level of chemical complexity COMs form, and to test at what molecular abundances COMs form.

We present detections and detailed column density analyses for multiple COMs towards the young starless core L1521E. In section 2 we discuss the line observations made by the Arizona Radio Observatory (ARO) 12m telescope. In section 3 we discuss our process for estimating the H_2 column density as well as the line analysis for each molecule detected. Included is a detailed description of non-detected transitions as well as discussion of glycoaldehyde (cis- CH_2OHCHO), which was targeted but not detected and known as an important molecule for building up sugars of astrobiological importance (see Jiménez-Serra et al. (2020)). We also calculate column densities and account for the beam filling factor. We then discuss how our results compare to other sites of low-mass star formation, as well as to modeled abundances, in section 4. Lastly, we summarize our results in section 5.

2 ARO 12M OBSERVATIONS

Molecular line observations were made with the ARO 12m telescope during three separate seasons, two years apart, using two different backend receivers. The first observing shifts between January 12,

2017 and April 27, 2017 with 10 tunings between 84 and 102 GHz (3.6 – 2.9mm). The sideband separating, dual polarization 3mm ALMA prototype receiver was used with the MAC backend in a mode with 300 MHz bandwidth with 48.8 kHz resolution (bandwidth of $880 - 1060 \text{km s}^{-1}$ with $0.14 - 0.17 \text{km s}^{-1}$ resolution). Two IFs within the same sideband were connected to the Vertical (Vpol) and Horizontal (Hpol) polarization feeds. The lower sideband was used for frequencies less than 97 GHz while the upper sideband was used for frequencies higher than 97 GHz. The rejection between sidebands was measured by injecting a tone into the opposite sideband and measuring the strength of the signal in the observed sideband. The sideband rejection was $\geq 18 \text{dB}$ for all tunings.

The second set of observing shifts took place between May 12th, 2019 and June 25th, 2019 with 3 different tunings on the 3mm receiver between 84 and 99 GHz (3.6 – 3.0mm), and 4 tunings on the 4mm receiver between 69 and 77 GHz (3.8 – 4.3mm). These observations used the new AROWS backend in a mode with 125 MHz bandwidth and 19.5 kHz resolution. There was a third set of observations that took place between February 17th and February 27th, 2019 utilizing the AROWS backend, tuned to the 79 GHz HCOOCH_3 transitions with the 4mm receiver.

Position-switched observations of L1521E were centered on the $850 \mu\text{m}$ dust continuum peak position of $4^{\text{h}} 29^{\text{m}} 14.9^{\text{s}} +26^{\text{d}} 13' 56.6'' \text{J2000.0}$, with 5 to 6 minutes total integration time (ON+OFF) between calibration scans (longer in good weather). During the first observing run, measurements of Venus and Mars were used to determine the average beam efficiency. Values were consistent for all 3mm tunings with an average value of $\eta_{\text{mb,MAC,3mm}} = 0.87 \pm 0.01$. Additionally, a factor of 1.14 needed to be multiplied to the final main beam temperature due to systematic calibration error present in the software of the MAC. The MAC antenna temperature was found to be 14% lower than the new more trusted AROWS backend (see Scibelli & Shirley (2020)). For the two remaining observing runs, AROWS was used and average beam efficiencies for the 3mm and 4mm observations were calculated separately. We note that during the Summer between the first observing run (MAC) and the second and third sessions (AROWS), the antenna surface accuracy was improved. During the second run, we used observations of just Mars to get an average value of $\eta_{\text{mb,AROWS,3mm}} = 0.91 \pm 0.01$ for all 3mm tunings. For the 4mm tunings, we average Venus, Mars and Jupiter measurements to determine an average beam efficiency of $\eta_{\text{mb,AROWS,3mm}} = 0.93 \pm 0.01$. In the third observing session, exclusively set to a 4mm tuning, the average beam efficiency was calculated to be $\eta_{\text{mb,AROWS,4mm}} = 0.92 \pm 0.01$, using Jupiter and Mars measurements.

Each tuning was chosen to include one or more COMs within the bandpass. Simple LTE, or local thermal equilibrium, excitation analyses were performed to estimate the most likely line to be observed in the 3mm(4mm) bandpass. In LTE the same excitation temperature is assumed for all transitions, which we have to assume is true because no collisional rates are available. In Scibelli & Shirley (2020) excellent agreement was found when both the LTE and non-LTE methods were applied to methanol, CH_3OH , which does have published collisional rates. Data reduction was performed using the CLASS program of the GILDAS package¹. The AROWS spectra have been hanning smoothed by two channels since the default software writes out the data at half the actual resolution.

¹ <http://iram.fr/IRAMFR/GILDAS/>

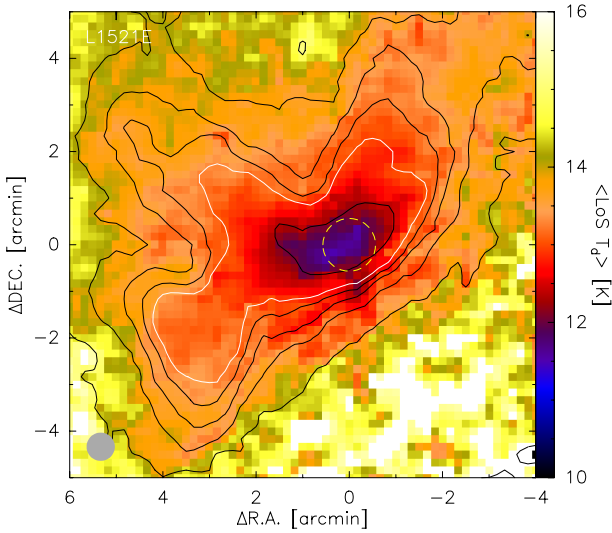


Figure 1. A map of the average line-of-sight dust temperature (color scale) and column density (contours) determined from SED fitting of *Herschel Space Observatory* observations at 250, 350, 500 μm centered on L1521E at $4^{\text{h}} 29^{\text{m}} 14.9^{\text{s}} +26^{\text{d}} 13' 56.6''$ J2000.0. The N_{H} contours correspond to 2, 4, 6, 8, 10, 20 $\times 10^{21} \text{ cm}^{-2}$ (for N_{H_2} , divide by 2). The yellow dashed circle indicates the average 12m beam size within which we find an average $\langle N_{\text{H}_2} \rangle = 1.6 \times 10^{22} \text{ cm}^{-2}$.

3 ANALYSIS AND RESULTS

3.1 Dust Continuum

Launhardt et al. (2013) developed a continuum pixel-by-pixel SED fitting technique to model the average line-of-sight dust temperature distribution and the H_2 column density (assuming a total gas mass to dust mass ratio of 150:1 and OH5 dust opacities, Ossenkopf & Henning (1994)) from *Herschel Space Observatory* and other FIR and submillimeter observations. L1521E was observed with MIPS on the *Spitzer Space Telescope* at 160 μm and with SPIRE on the *Herschel Space Observatory* at 250, 350, and 500 μm . Unfortunately, no PACS observations of L1521E exist. MIPS observations have severe instrumental artifacts that prohibit detailed, pixel-by-pixel modeling of that image but a total flux may be used as a constraint when modeling the integrated SED (Kirk et al. 2007). L1521E was also observed with SCUBA at the 15m JCMT (Kirk et al. 2005), but this map was too small to recover the emission level from the extended envelope and could therefore not easily be combined with the *Herschel* data. The data reduction, including color corrections, of the *Herschel*/SPIRE data is described in Launhardt et al. (2013). The results of SED modeling the archival *Herschel* data are shown in Figure 1.

The central regions of L1521E have peak column densities of $N_{\text{H}} = 3.9 \times 10^{22} \text{ cm}^{-2}$ and average line-of-sight dust temperatures of 11 K. The average H_2 density within the typical 12m beam size of $1'$ (corresponding to $\sim 8400 \text{ AU}$ at 140 pc) is $N_{\text{H}_2} = 1.6 \times 10^{22} \text{ cm}^{-2}$. We used this average H_2 column density for all subsequent calculations of molecular abundances. The corresponding mass is $2.2 M_{\odot}$. Our SPIRE image modeling results are consistent within a factor of two in column density with the analysis of SPIRE-FTS observations by Makiwa et al. (2016).

Using the 850 μm JCMT map and the same techniques and grid of radiative transfer models described in Shirley et al. (2005), we find that a thermally-supported Bonnor-Ebert sphere with a central density of $3 \times 10^5 \text{ cm}^{-3}$ is the best-fitted model. This result is con-

sistent with our archival *Herschel* SED modeling and the published radiative transfer modeling of MAMBO 1.2 mm data from Tafalla & Santiago (2004) ($n(r) = 2.7 \times 10^5 \text{ cm}^{-3} / [1 + (r/6.3 \times 10^{16} \text{ cm})^2]$). We use these density profiles to calculate the virial parameter, $\alpha_{\text{vir}} = 3R\sigma_v^2/a_1GM(R)$. The line-of-sight velocity dispersion, $\sigma_v = 0.25 \pm 0.02 \text{ km s}^{-1}$, is calculated from the average and standard deviation of the observed linewidths toward the dust continuum peak in Nagy et al. (2019) and is corrected for the molecule specific thermal broadening and the sound speed (Fuller & Myers 1992). The density profile correction factor, a_1 , is calculated using the techniques described in the appendices of Bertoldi & McKee (1992) and Sipilä et al. (2011). The exact radius of L1521E is uncertain and depends on how the core boundary is defined (i.e. for examples of various definitions see Benson & Myers 1989; Pattle et al. 2015; Seo et al. 2015; Chen et al. 2019). Assuming that it is in between angular radii of $60''$ to $140''$, then we find that α_{vir} is between 1.8 – 0.9 which would indicate that L1521E is near the typical dividing line between a starless core and a gravitationally-bound prestellar core. We shall continue to use the more general term starless when referring to the L1521E core.

3.2 Molecular Identifications

With confidence, we report the first detection of CH_3OCH_3 , HCOOCH_3 and CH_2CHCN in the young starless core L1521E. Additionally, eight transitions of CH_3CHO and seven transitions of CH_2CHCN were detected, each set used to construct rotation diagrams to constrain excitation temperature and column density. The properties of the observed lines are listed in Table 1. For each transition, we calculated the integrated intensity over the line and its uncertainty from the following equation,

$$I \pm \sigma_I = \sum_i T_i \delta v_{ch} \pm \sigma_T \sqrt{\frac{3\Delta v_{\text{FWHM}} \delta v_{ch}}{\sqrt{2 \ln 2}}}, \quad (1)$$

where δv_{ch} is the spectrometer velocity resolution, and σ_T is the baseline rms. The integrated intensity and uncertainty are calculated over a velocity range corresponding to the $\pm 3\sigma$ width of a Gaussian with the same integrated intensity. This technique works well for lines that are Gaussian and do not have significant skewness (for instance due to outflows), which is the case for all lines observed toward L1521E. The median FWHM for our lines is at 0.35 km s^{-1} (see Table 2). We note that in Table 2 there is slight discrepancy in v_{LSR} for the two transitions of CH_2CHCN which were detected with the old (less trustworthy) MAC backend receiver. Otherwise, the v_{LSR} of the remaining lines lie at $\sim 7 \text{ km s}^{-1}$ (median value of 6.97 km s^{-1}). In the following subsections we present an overview of the molecules detected.

Table 1. Complex Organic Molecule Fit Results

Molecule	Transition	ν (GHz)	E_{ul}/k (K)	$^a g_{ul}$	A_{ul} (s^{-1})	T_{mb} (mK)	$\sigma(T_{mb})$ (mK)	$I(T_{mb})$ (mK km s $^{-1}$)	$\sigma(I)$ (mK km s $^{-1}$)
CH ₃ CHO	3 _{1,3} – 2 _{0,2} A*	101.89241	7.7	14	4.0E-06	23.0	4.0	10.7	1.3
	5 _{0,5} – 4 _{0,4} A	95.96347	13.8	22	3.0E-05	89.0	9.0	30.0	2.0
	5 _{0,5} – 4 _{0,4} E	95.94744	13.9	22	3.0E-05	51.0	8.0	23.0	2.0
	2 _{1,2} – 1 _{0,1} A	84.21975	5.0	10	2.4E-06	23.0	4.0	7.1	0.8
	4 _{0,4} – 3 _{0,3} A	76.87895	9.2	18	1.5E-05	89.0	11.0	36.0	3.0
	4 _{0,4} – 3 _{0,3} E	76.86644	9.3	18	1.5E-05	103.0	10.0	41.0	3.0
	4 _{1,4} – 3 _{1,3} A	74.89168	11.3	18	1.3E-05	53.0	11.0	14.0	2.0
	4 _{1,4} – 3 _{1,3} E	74.92413	11.3	18	1.3E-05	48.0	9.0	13.0	2.0
CH ₃ OCH ₃	4 _{1,4} – 3 _{0,3} AA	99.32607	10.2	90	5.5E-06	9.1	3.0	2.9	0.6
	4 _{1,4} – 3 _{0,3} EE	99.32522	10.2	144	5.5E-06	10.0	3.0	4.2	0.7
	4 _{1,4} – 3 _{0,3} AE+EA	99.32436	10.2	90	5.5E-06	4.6	3.0	5.5	1.2
	4 _{2,3} – 4 _{1,4} EE*	93.85710	14.7	144	3.6E-06	...	2.0	...	0.8
HCOOCH ₃	2 _{2,1} – 2 _{1,2} EE*	89.69981	8.4	80	2.3E-06	...	2.0	...	0.8
	8 _{1,8} – 7 _{1,7} A*	89.31664	20.1	34	1.0E-05	...	4.0	...	1.3
	8 _{1,8} – 7 _{1,7} E*	89.31466	20.2	34	1.0E-05	...	4.0	...	1.3
	7 _{0,7} – 6 _{0,6} A	79.78389	15.7	30	7.2E-06	11.0	3.0	6.4	0.6
CH ₂ CHCN	7 _{0,7} – 6 _{0,6} E	79.78171	15.7	30	7.2E-06	12.0	3.0	3.9	0.9
	11 _{0,11} – 10 _{0,10}	103.57539	29.9	69	8.8E-05	...	3.0	...	0.6
	10 _{1,9} – 9 _{1,8}	96.98245	27.8	63	7.2E-05	14.0	3.0	4.8	0.6
	10 _{0,10} – 9 _{0,9}	94.27664	24.9	63	6.2E-05	27.0	4.0	8.0	0.9
	10 _{1,10} – 9 _{1,9}	92.42626	26.6	63	6.8E-05	18.0	3.0	4.4	0.6
	5 _{1,5} – 4 _{0,4} *	89.13091	8.8	33	1.8E-06	...	2.0	...	0.8
	9 _{1,8} – 8 _{1,7} *	87.31281	23.1	57	5.3E-05	24.0	5.0	9.9	1.9
	9 _{0,9} – 8 _{0,8} *	84.94600	20.4	57	4.9E-05	30.0	4.0	12.0	1.7
	8 _{1,7} – 7 _{1,6}	77.63384	18.9	51	3.6E-05	37.0	5.0	12.5	1.3
	8 _{0,8} – 7 _{0,7}	75.58569	16.3	51	3.4E-05	50.0	5.0	16.9	1.3
cis-CH ₂ OHCHO	5 _{2,4} – 4 _{1,3} *	87.76453	10.7	11	8.6E-06	...	4.0	...	1.4
	8 _{1,8} – 7 _{0,7} *	85.78224	18.9	17	1.5E-05	...	3.0	...	1.2
	8 _{0,8} – 7 _{1,7} *	82.47067	18.8	17	1.3E-05	...	4.0	...	1.3

Note. — *Transitions targeted with the MAC backend. ^aValues for CH₃CHO and HCOOCH₃ from JPL catalog² (Pickett et al. 1998) and for the remaining transitions from CDMS database³ (Müller et al. (2001), Müller et al. (2005), Endres et al. (2016)). We note that A_{ul} can be calculated by the following equation, $A_{ul} = (64\pi^4 \nu_i^3 / 3hc^3) (S\mu^2 / (2J' + 1))$, where J' is the upper J in the transition and line strength, S , can be interpolated from values tabulated in Standards & Wacker (1969).

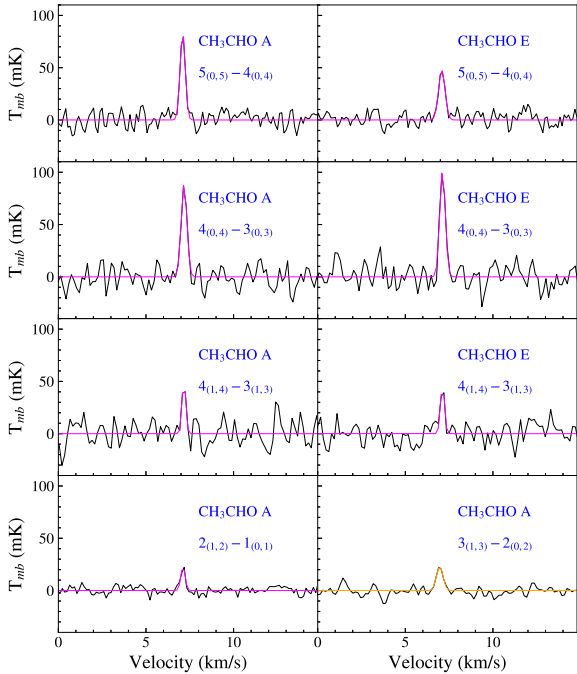


Figure 2. Spectra of all eight CH₃CHO transitions detected. In all panels except the bottom right the gaussian fits are overplotted in magenta, for those detected with the AROWS backend receiver. In the bottom right plot the gaussian fit is overplotted in orange and was observed with the MAC backend receiver. Each line peaks at the v_{LSR} ($\sim 7 \text{ km s}^{-1}$) of L1521E.

3.2.1 Acetaldehyde (CH₃CHO)

A total of eight transitions of CH₃CHO were detected by tuning to 3mm and 4mm rotational transitions suitable for 10 K gas, i.e., those with values for $E_u/k < 15 \text{ K}$ (spectroscopic work detailed in Kleiner et al. (1996)). Observed spectra are plotted in Figure 2. With both the MAC and the AROWS backends, we observed the 96 GHz $5_{0,5} - 4_{0,4}$ A and E transitions, however we only report on the AROWS detection here. The weak CH₃CHO $3_{1,3} - 2_{0,2}$ A transition at 101.89 GHz was detected with only the MAC. The remaining transitions were detected exclusively with the AROWS backend, at $\sim 0.07\text{--}0.08 \text{ km s}^{-1}$ resolution. The weakest transition, CH₃CHO A $2_{1,2} - 1_{0,1}$ at 84 GHz, was targeted and detected with 4σ confidence. The remaining transitions, each various K levels of $J=4-3$ (refer to Figure 3), were targeted with the 4mm receiver. The 76.9 GHz, $4_{0,4} - 3_{0,3}$ transitions are brightest. Each A & E pair were observed in the same bandpass. For the 95.95 GHz A and E states they have a ratio of around 9:5, unlike the 76.9 and 74.9 GHz transitions with ratios close to the LTE statistical ratio of 1:1. Observations of A to E ratios of 1:1 have been observed towards other sources (Bacmann et al. 2012; Taquet et al. 2017).

3.2.2 Dimethyl Ether (CH₃OCH₃)

A simple LTE excitation analysis of CH₃OCH₃ shows that the $4_{1,4} - 3_{0,3}$ transition at 99.325 GHz should be the strongest line in the 3mm band for gas at 10 K (spectroscopic work detailed in Neustock et al. (1990)). Furthermore, the upper state energy level ($J_{K_a, K_c} = 4_{1,4}$) can only radiate (via electric dipole radiation) through this single transition (see Figure 4). For CH₃OCH₃ there is an advantage of having torsional splitting of the rotational levels, as the lines manifest

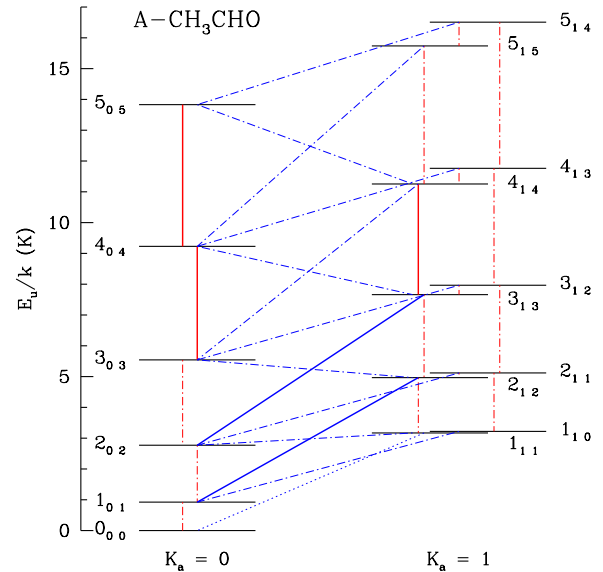


Figure 3. The rotational energy level diagram for CH₃CHO A. Solid red lines connect a-type ($\Delta K_a = 0, \Delta K_c = \pm 1$) transitions and solid blue lines connect b-type ($\Delta K_a = \pm 1, \Delta K_c = \pm 1$) transitions. Each solid line represents those transitions detected in L1521E. See Figure 2 in Gilmore et al. 1976 for a more complete energy level diagram.

as three closely spaced lines ($\sim 2 \text{ MHz}$) with LTE statistical weights of 1:2:1 that are in a distinct, easy to identify pattern.

We observed CH₃OCH₃ during both observing sessions, further verifying its detection. A 93 hour (total observing time), multi-shift integration with baseline rms of 1.9 mK using the MAC backend was successful in detecting the $4_{1,4} - 3_{0,3}$ transition (right panel of Figure 5), with three distinct peaks of signal-to-noise > 6 in integrated intensity at the correct frequencies for the AA, EE, and AE+EA species of CH₃OCH₃. During the second round of observations we integrated for 166 hours, down to an rms of 3.0 mK with the AROWS backend, confirming the previous MAC spectrometer detection (left panel of Figure 5). The EE species is the brightest line detected with $\sim 4\sigma$ confidence. By re-observing with AROWS we gained higher spectral resolution, resolving linewidths. Values from the AROWS observation are reported in Table 1.

Attempts to detect the $4_{2,3} - 4_{1,4}$ and $2_{2,1} - 2_{1,2}$ transitions of CH₃OCH₃ during the first observing run were unsuccessful despite a baseline rms value of 2.2 mK for both lines. We calculate a 3σ upper limit to the integrated intensity of 0.8 mK km s^{-1} , assuming the same FWHM linewidth as observed for the $4_{1,4} - 3_{0,3}$ EE transition that was observed with the MAC backend, i.e., $\text{FWHM} = 0.42 \text{ km s}^{-1}$. Each of the upper states of these transitions have multiple possible routes to radiate to lower energy levels. The transitions targeted in the 3mm band do not have the largest branching ratio among those transitions, which mitigate their intensity (refer to Figure 4).

3.2.3 Methyl Formate (HCOOCH₃)

Methyl formate, written as HCOOCH₃ or CH₃OCHO, was detected in the 4mm band but not in the 3mm band (spectroscopic work detailed in Ilyushin et al. (2009)). We find the 76 GHz transitions are more favorable for detection in cold L1521E, in part due to the lower upper energies ($E_u/k = 15.7 \text{ K}$), when compared to the 89 GHz transitions ($E_u/k = 20 \text{ K}$). We report detections of the 79 GHz

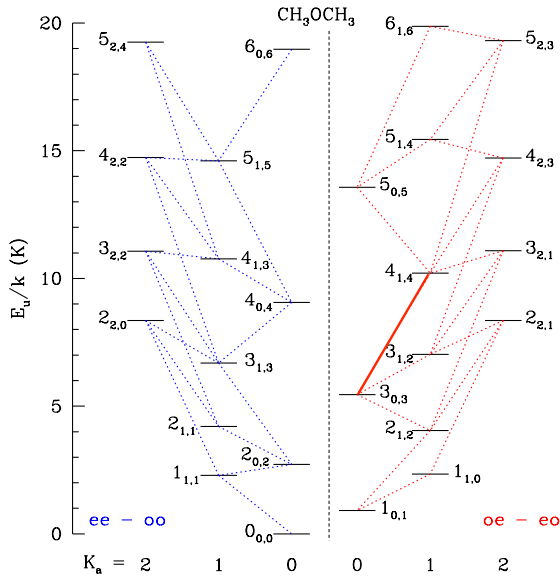


Figure 4. The rotational energy level diagram for CH_3OCH_3 EE with only the stronger b-type transitions shown ($\Delta K_a = \pm 1$, $\Delta K_c = \pm 1$). Weaker c-type transitions are not shown ($\Delta K_a = \pm 1$, $\Delta K_c = 0$). A solid red line connects the $4_{1,4}$ and $3_{0,3}$ levels, which produces the CH_3OCH_3 EE transition detected in L1521E.

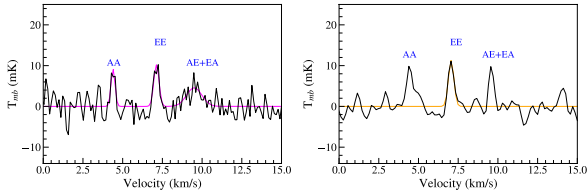


Figure 5. CH_3OCH_3 observations from first observing run with the MAC backend (right) and the second observing run with the new AROWS backend (left), at a higher velocity resolution. The center EE transition peaks at the v_{LSR} of L1521E.

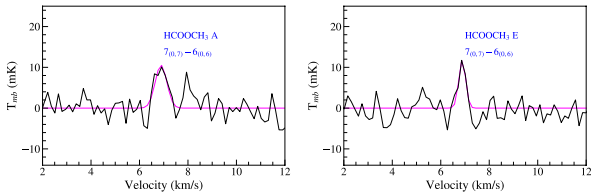


Figure 6. Two transitions of the 79 GHz $7_{0,7} - 6_{0,6}$ A and E states of HCOOCH_3 detected in L1521E, centered on the v_{LSR} of L1521E.

$7_{0,7} - 6_{0,6}$ A and E transitions (observed in the same bandpass), reported with 3σ confidence (Figure 6). The 89 GHz $8_{1,8} - 7_{1,7}$ A and E transitions of HCOOCH_3 have been detected before (see [Taqet et al. \(2017\)](#)), yet we only report upper limits in Table 1 after getting down to rms of 3.5 mK.

3.2.4 Vinyl Cyanide (CH_2CHCN)

Seven transitions of vinyl cyanide (CH_2CHCN) were detected and plotted in Figure 7 (spectroscopic work detailed in [Costain & Stoich-](#)

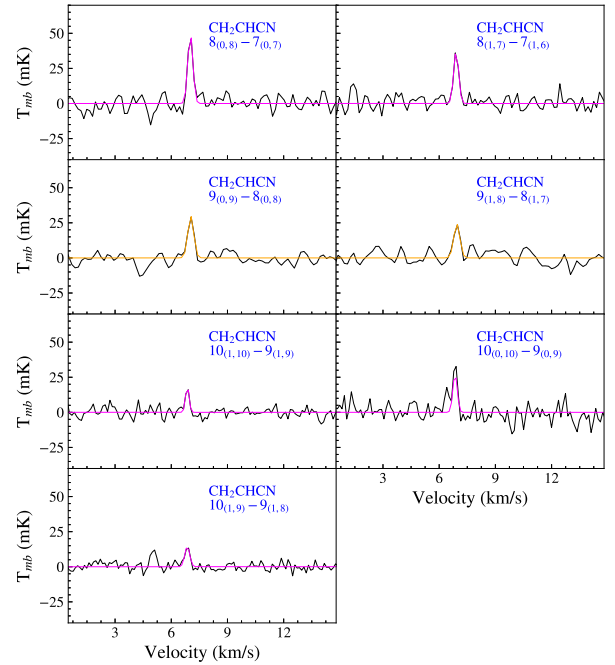


Figure 7. Spectra of seven separate transitions of CH_2CHCN . We note that the $J = 9 - 8$ transitions were detected earlier with the MAC and the gaussian fit is displayed in orange. Each transition is centered on the v_{LSR} of L1521E.

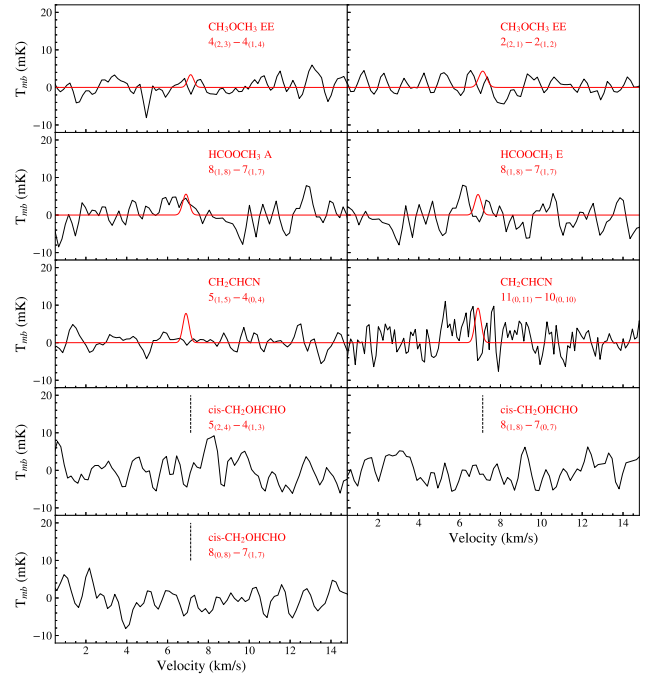


Figure 8. Spectra showing the non-detected transitions as detailed in Table 1. For the non-detected transitions for which we have column density estimates for, their modeled Gaussian LTE spectrum is plotted in red. The attempt to detect the CH_2CHCN $11_{0,11} - 10_{0,11}$ transition done with AROWS backend and therefore has higher velocity resolution, all others were attempted with the MAC backend. For $\text{cis-CH}_2\text{OHCHO}$, which was not detected in any transition, a vertical dashed line annotates where we would expect the line to appear, centered on the v_{LSR} of L1521E.

eff (1959)). Another two transitions were not detected, and we report upper limits in Table 1. CH₂CHCN is the most complex organic molecule we detect with a nitrogen atom. The strongest transition detected is the 8_{0,8} – 7_{0,7} a-type transition, with 8 σ confidence. The 9_{0,9} – 8_{0,8} transition is the second strongest, and the 9_{1,8} – 8_{1,7} transition is slightly weaker.

Since the upper state of the two 9 – 8 transitions from MAC observations have similar energies (20.4 K and 23.1 K respectively), they do not give a strong constraint on T_{ex}. The non-detection of the weaker 5_{1,5} – 4_{0,4} b-type transition with a much lower upper energy state (E_u/k = 8.8 K), does give a 3 σ upper limit and constrains T_{ex} > 5K. This is higher than the excitation temperatures we derive for CH₃CHO, but perhaps not surprising since we detected even higher energy transitions, up to 10_{1,9} – 9_{1,8} with an upper energy of E_u/k = 27.8 K.

We note that CH₂CHCN was recently detected and mapped in Titan’s atmosphere with ALMA (Lai et al. 2017). Of astrobiological interest, CH₂CHCN is thought to be important as a potential molecule to form membranes in Titan’s liquid methane oceans.

3.3 Molecular Non-Detections

Mock integrated intensity values for transitions of CH₃OCH₃, HCOOCH₃ and CH₂CHCN that were not detected were calculated based on the column density calculated from the detected transitions and assuming the same T_{ex} (and f_v = 1). We also plot the LTE modeled gaussian fits over the spectra in Figure 8. For CH₃OCH₃ the 3 σ upper limit to the integrated intensity is 2.4 mK km s⁻¹. The simulated integrated intensity for the 4_{2,3} – 4_{1,4} transition, assuming the same excitation temperature of 4.5 K, is below this limit at 1.1 mK km s⁻¹. Similarly, the simulated integrated intensity for the 2_{2,1} – 2_{1,2} transition was 1.7 mK km s⁻¹, below the 3 σ upper limit. For both 8_{1,8} – 7_{1,7} transitions of HCOOCH₃, a 3 σ upper limit to the integrated intensity is calculated to be 3.9 mK km s⁻¹. The simulated integrated intensities fall below this 3 σ upper limit, at 1.9 mK km s⁻¹.

In the case of CH₂CHCN, a 3 σ upper limit to the integrated intensity is calculated to be 2.4 mK km s⁻¹ for the 5_{1,5} – 4_{0,4} transition of CH₂CHCN. The simulated integrated intensity assuming the same excitation temperature of 5 K was 2.5 mK km s⁻¹, which is just at our detection limit. For the 11_{0,11} – 10_{0,11} transition of CH₂CHCN a 3 σ upper limit to the integrated intensity is calculated to be 1.8 mK km s⁻¹. The simulated integrated intensity assuming the same excitation temperature of 5 K was 2.9 mK km s⁻¹, which should have been detected by our observations at the 5 σ level. Yet, looking at Figure 8, we see that there is too much noise to confirm a detection. Also note the detection of this transition was attempted with the new AROWS backend and therefore has higher velocity resolution, all others were attempted with the MAC backend.

3.3.1 Glycoaldehyde (cis-CH₂OHCHO)

We attempted to detect three separate transitions of cis-CH₂OHCHO but were unsuccessful. The detection limits are reported in Table 1 and spectra plotted in Figure 8 (spectroscopic work detailed in Marstokk & Møllendal (1970) and Butler et al. (2001)). An especially interesting molecule to target, CH₂OHCHO is one of the simplest sugars (Marstokk & Møllendal 1973), and a constitutional isomer of both acetic acid (CH₃COOH) and the more ubiquitous HCOOCH₃. First detected towards Sagittarius B2(N) (Hollis et al. 2000), as well as toward the high-mass hot core G31.41+0.31 (Beltrán et al. 2009),

CH₂OHCHO is likely to form mainly through surface reactions on interstellar dust grains in which HCO is an important constituent (see Butscher et al. (2015); Rivilla et al. (2019); Simons et al. (2020)). To date, cis-CH₂OHCHO has not been detected toward a starless core.

3.4 Column Density Calculations

For CH₃CHO, since the upper energy levels of the five detected A transitions span from 5.0 – 13.9 K, we derive meaningful limits on the excitation temperature and column density. When performing this analysis we became concerned with source size and filling fraction errors that go into these types of calculations. We include filling fraction as a parameter that goes into the column density measurement as follows,

$$N_u = \frac{I}{hA_{ul}f_v} \frac{u_v(T_{\text{ex}})}{[J_v(T_{\text{ex}}) - J_v(T_{\text{cmb}})]}, \quad (2)$$

where f_v is the frequency (or transition) dependent filling fraction, I is the integrated intensity of the line, and u_v (Planck energy density) and J_v (Planck function in temperature units) are defined as,

$$u_v \equiv \frac{8\pi h\nu^3}{c^3} \frac{1}{\exp(h\nu/kT) - 1}, \quad (3)$$

$$J_v \equiv \frac{h\nu}{k} \frac{1}{\exp(h\nu/kT) - 1}. \quad (4)$$

In order to get the total column density (N_{tot}) from the upper state value (N_u), the Boltzmann equation in the CTEX (constant excitation temperature) approximation is used,

$$\frac{N_u}{g_u} = \frac{N_{\text{tot}}}{Q(T_{\text{ex}})} \exp(-E_u/kT_{\text{ex}}), \quad (5)$$

where Q(T_{ex}) is the partition function that depends on excitation temperature, E_u is the upper energy, and g_u the upper state degeneracy. Rotation diagrams are constructed to get estimates for N_{tot} and T_{ex} (right panel of Figure 9).

Since T_{ex} is still a variable in these equations, an iterative fit is performed where a first a guess at T_{ex} is made, and then adjusted depending on the slope of the fit, until both values merge. The partition function, Q(T_{ex}), is calculated independently from lists of the rotational energy levels (see section 7 and equation 54 in Mangum & Shirley (2015)).

Most calculations in the literature need to assume a filling fraction, f_v, of 1 since source size is not known a priori. The f_v parameter is related to both the beam size, which depends on the frequency of the transition observed, and the source size, which, for our purposes, is assumed to be the same for each transition for each oxygen bearing COM molecule. Assuming that the source intensity profile (I(θ)) and the telescope main beam pattern (P_n(θ)) can both be approximated by a Gaussian distribution, then

$$f_v = \frac{\int I(\theta)P_n(\theta)d\Omega}{I(\theta=0) \int P_n(\theta)d\Omega} = \frac{\theta_s^2}{\theta_b^2 + \theta_s^2}, \quad (6)$$

where θ_s is the source FWHM size and θ_b is the 12m FWHM beam size at the frequency of the transition. In the left panel of Figure 9 we plot how rotation curve fitted N_{tot} and T_{ex} change with source size for CH₃CHO. For example, at a source size of 57'' (orange line), the purple curve gives the same N_{tot} value as the ‘‘Corrected Source Size’’ fit in blue in the right panel of Figure 9. With an average beam size for all five transitions at ~ 70'', if our filling fraction is less than one, i.e. the source size is smaller than 70'', then N_{tot} will increase

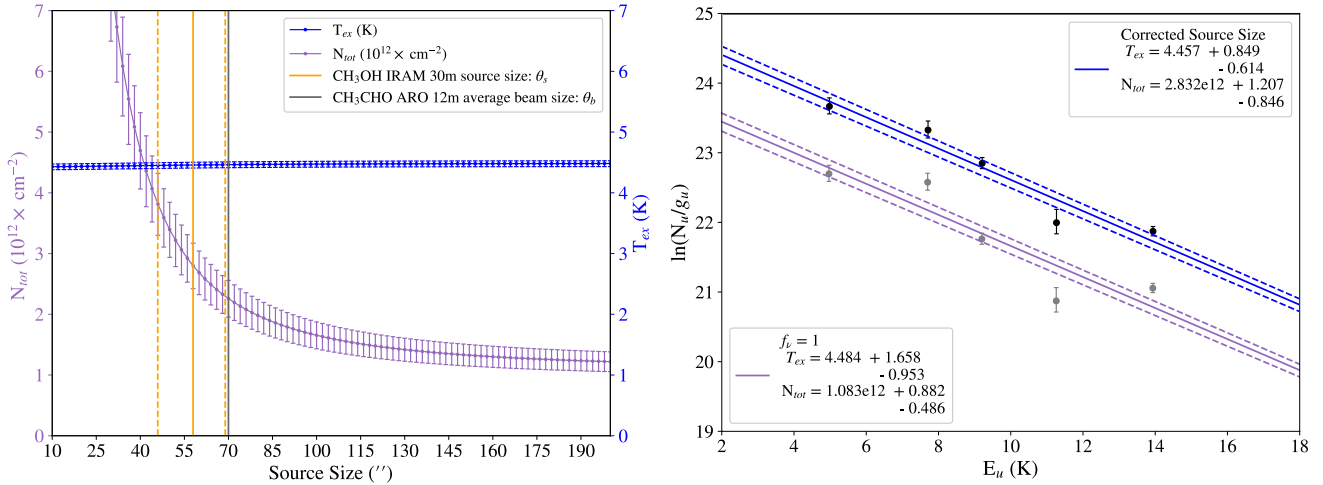


Figure 9. (left) The range of CH₃CHO A column densities as a function of source size is plotted as a purple curve with corresponding values on the left side of the y-axis. The shallow sloping blue line represents the range of CH₃CHO A excitation temperature as a function of source size with the corresponding values plotted on the right side of the y-axis. The orange line represents the source size calculated from a CH₃OH map of L1521E (Nagy et al. 2019), and dashed lines an uncertainty window of 20% (see section 3.5). At this source size of 57'' (orange line), the purple curve gives the same N_{tot} value as the “Corrected Source Size” fit in the right panel. The grey line at 70'' is the average 12m beam size for all CH₃CHO transitions detected. (right) Rotation diagram for CH₃CHO A showing the difference found if a filling fraction of 1 is assumed (grey points, purple fit) versus if the filling fraction is calculated correctly using the beam and source sizes (black points, blue fit). Instead of errors based on solely the maximum and minimum fit from observed intensity uncertainties (the dashed lines), a least squares analysis is done to find more realistic errors to our linear fit.

strongly with smaller source sizes. The excitation temperature, T_{ex} , in contrast, is nearly independent of source size when beam sizes are kept consistent for one telescope dish diameter.

In order to estimate a source size, we use a CH₃OH map from Nagy et al. (2019) observed with the IRAM 30m telescope. They do have a CH₃CHO map, however the lines were not detected with high enough sensitivity ($rms \sim 30$ mK) to accurately match emission morphology. We know CH₃OH is one of the simplest and most abundant of the COMs and thus traces the extended COM structure of L1521E. Additionally, CH₃OH and CH₃CHO are thought to be linked chemically (see discussion in Scibelli & Shirley (2020)). The area within the FWHM of the peak brightness in the CH₃OH map corresponds to a diameter of 62.9'' (source convolved with the IRAM 30m beam; $\theta_{\text{src} \times \text{IRAM}}$). When subtracted off in quadrature from the beam size of IRAM at the frequency of CH₃OH ($\theta_{\text{IRAM}} = 25.6''$), source size is found by,

$$\theta_{\text{src} \times \text{IRAM}}^2 = \theta_s^2 + \theta_{\text{IRAM}}^2 \quad (7)$$

The source size is estimated to be $\theta_s = 57''$ (see section 3.5 for uncertainties). When assuming $f_v = 1$, N_{tot} is underestimated by a factor of 2.6, compared to when f_v is corrected given the proper source size (Figure 9, right). Errors in the fit are calculated from a least square fitter. Our range of column densities for CH₃CHO A, reported in Table 3, correcting for source size, is then $N_{\text{tot}} = 1.98 - 4.04 \times 10^{12} \text{ cm}^{-2}$. If $f_v = 1$ is assumed we find $N_{\text{tot}} = 0.59 - 1.96 \times 10^{12} \text{ cm}^{-2}$. In the right panel of Figure 9 we also note that for $f_v = 1$ there is more scatter away from the linear fit compared to the data points plotted with the corrected source size. Without filling fraction corrections, column densities are underestimated.

For both CH₃OCH₃ and HCOOCH₃ the excitation temperatures calculated from our CH₃CHO analysis ($T_{\text{ex}} = 4.46$ K, 4.48 K) are used to derive total column densities. In order to estimate possible uncertainties introduced by this assumption, we calculate column

densities given a lower T_{ex} value (at 4.0 K) and a higher T_{ex} value (at 5.5 K), finding a $\sim 15\%$ increase and decrease, respectively, in column density, which is within our range of error. In the case of CH₃OCH₃, we only consider the well detected (4σ) EE state transition. Correcting for source size (assuming the same spatial distribution as CH₃OH), a plausible range of column densities are found, $N_{\text{tot}} = 1.32 - 1.86 \times 10^{12} \text{ cm}^{-2}$. This corresponds to abundances $X(\text{CH}_3\text{OCH}_3/\text{H}_2) = 0.82 - 1.16 \times 10^{-10}$ (see Table 3). In the case of HCOOCH₃, E state transitions went into the column density analysis, which gives a plausible range $N_{\text{tot}} = 3.44 - 5.48 \times 10^{12} \text{ cm}^{-2}$, for corrected source size. This corresponds to an abundance of $X(\text{HCOOCH}_3/\text{H}_2) = 2.14 - 3.42 \times 10^{-10}$. In Table 3 column densities are also calculated for CH₃OCH₃ and HCOOCH₃ when $f_v = 1.0$ is assumed.

Unfortunately, for CH₂CHCN we are not able make the assumption that CH₃OH traces the same spatial structure in L1521E. Compared to oxygen bearing COMS, we would expect molecules with nitrogen to peak at different locations on the core since molecules such as CO and N₂H⁺ are observed to peak differently in starless and prestellar cores (e.g., Bacmann et al. (2002); Lippok et al. (2013); see also Jiménez-Serra et al. (2016)). As a check, if we assume the same source size as for the oxygen bearing COMS we find $T_{\text{ex}} < 5$ K, supporting that the assumption is inaccurate. We could have used a simpler nitrogen-bearing COM, such as a CH₃CN map from Nagy et al. (2019), to estimate source size, but this map is too noisy for our purposes ($rms \sim 30$ mK). The seven transitions of CH₂CHCN that were detected, as well as two upper limit constraints, are used to construct a rotation diagram in the similar manner as done for CH₃CHO, assuming $f_v = 1$ (Figure 10). The 3σ integrated intensity values for the non-detection’s better constrain our fit, due to the extremes in E_u/k at 8.8 K and 29.9 K for the 89 GHz and 103 GHz lines, respectively. We find an excitation temperature of $T_{\text{ex}} = 5.02^{+0.39}_{-0.33}$ K and range of column densities from $N_{\text{tot}} = 0.73 - 1.37 \times 10^{12} \text{ cm}^{-2}$.

Table 2. Line FWHM and v_{LSR}

Molecule	Transition	ν (GHz)	FHWM km s ⁻¹	v_{LSR} km s ⁻¹
CH ₃ CHO	3 _{1,3} – 2 _{0,2} A*	101.89241	0.44[0.07]	6.96[0.03]
	5 _{0,5} – 4 _{0,4} A	95.96347	0.42[0.05]	7.10[0.02]
	5 _{0,5} – 4 _{0,4} E	95.94744	0.50[0.08]	7.08[0.03]
	2 _{1,2} – 1 _{0,1} A	84.21975	0.29[0.07]	7.10[0.02]
	4 _{0,4} – 3 _{0,3} A	76.87895	0.38[0.05]	7.18[0.02]
	4 _{0,4} – 3 _{0,3} E	76.86644	0.37[0.04]	7.12[0.02]
	4 _{1,4} – 3 _{1,3} A	74.89168	0.24[0.11]	7.16[0.03]
	4 _{1,4} – 3 _{1,3} E	74.92413	0.27[0.10]	7.12[0.03]
CH ₃ OCH ₃	4 _{1,4} – 3 _{0,3} AA	99.32607	0.30[0.07]	6.97[0.03]
	4 _{1,4} – 3 _{0,3} EE	99.32522	0.39[0.07]	7.13[0.04]
	4 _{1,4} – 3 _{0,3} AE+EA	99.32436	1.14[0.34]	6.93[0.14]
HCOOCH ₃	7 _{0,7} – 6 _{0,6} A	79.78389	0.57[0.09]	6.96[0.05]
	7 _{0,7} – 6 _{0,6} E	79.78171	0.32[0.08]	6.89[0.04]
CH ₂ CHCN	10 _{1,9} – 9 _{1,8}	96.98245	0.31[0.06]	6.85[0.03]
	10 _{0,10} – 9 _{0,9}	94.27664	0.27[0.06]	6.85[0.02]
	10 _{1,10} – 9 _{1,9}	92.42626	0.22[0.06]	6.86[0.02]
	9 _{1,8} – 8 _{1,7} *	87.31281	0.38[0.07]	6.26[0.03]
	9 _{0,9} – 8 _{0,8} *	84.94600	0.37[0.05]	6.55[0.02]
	8 _{1,7} – 7 _{1,6}	77.63384	0.31[0.05]	6.91[0.02]
	8 _{0,8} – 7 _{0,7}	75.58569	0.32[0.04]	7.02[0.02]

Note. — *Transitions targeted with the MAC backend.

Table 3. Column Densities and Abundances

Species:	CH ₃ CHO A	CH ₃ OCH ₃ EE	HCOOCH ₃ E	CH ₂ CHCN	cis-CH ₂ OHCHO
Corrected Source Size					
T_{ex} (K)	4.46 ^{+0.85} _{-0.61}	4.46	4.46
N_{tot} (10 ¹² cm ⁻²)	2.83 ^{+1.21} _{-0.85}	1.59 ^{+0.27} _{-0.27}	4.46 ^{+1.02} _{-1.02}
*X wrt. H ₂ (10 ⁻¹⁰)	1.77 ^{+0.76} _{-0.53}	0.99 ^{+0.17} _{-0.17}	2.78 ^{+0.64} _{-0.64}
$f_{\nu} = 1$					
T_{ex} (K)	4.48 ^{+1.66} _{-0.95}	4.48	4.48	5.02 ^{+0.38} _{-0.33}	4.5
N_{tot} (10 ¹² cm ⁻²)	1.08 ^{+0.88} _{-0.49}	0.74 ^{+0.13} _{-0.13}	1.60 ^{+0.37} _{-0.37}	1.00 ^{+0.37} _{-0.27}	< 1.84
*X wrt. H ₂ (10 ⁻¹⁰)	0.68 ^{+0.25} _{-0.18}	0.46 ^{+0.08} _{-0.08}	1.00 ^{+0.23} _{-0.23}	0.62 ^{+0.55} _{-0.31}	< 1.15

Note. — *Calculated using the average H₂ column density of $N_{\text{H}_2} = 1.6 \times 10^{22}$ cm⁻². Note: The excitation temperature, T_{ex} , derived for CH₃CHO is assumed for all other oxygen-bearing species.

3.5 Analysis of Uncertainties

We produce χ^2 parameter-space plots for the determination of column density and excitation temperature from CH₃CHO A transitions. By re-arranging equations 2 and 5 we estimate how well the calculated line intensities fit with the observed data for each set of parameters (θ_s , T_{ex} , N) by calculating,

$$\chi^2 = \sum_{i=1}^n \left(\frac{I_i^{\text{obs}} - I_i^{\text{calc}}}{\sigma_i^{\text{obs}}} \right)^2, \quad (8)$$

where n is the number of transitions observed, which is 5 in our case, I_i^{obs} is the observed integrated intensity, I_i^{calc} is the integrated line intensity predicted by the equations, and σ_i^{obs} is the uncertainty associated with the observed line integrated intensity. In the top panel of Figure 11 we plot χ^2 as a function of the CH₃CHO A column density and source size (T_{ex} set to 4.46 K), and similarly in the bottom panel χ^2 as a function of the CH₃CHO A column density and T_{ex} (source size set to 57"). In general, as column density increases, better fits (lower χ^2 values) can be found for small source size and low excitation temperatures. The black dashed lines in Figure 11 represent the calculated values from our rotation diagram analysis, which cross the minimized portion of the curve where $\chi^2 < 15$. Within this region ($\chi^2 < 15$), excitation temperature is constrained to be between 4.2 – 5.5 K and N_{tot} between $1.5 - 3.5 \times 10^{12} \text{ cm}^{-2}$, comparable to the uncertainty range from our rotation diagram analysis (blue fit in right panel of Figure 9). Source size, however, is not as well constrained since it is minimized asymptotically with increasing column densities given source sizes $15'' < \theta_s < 74''$.

Since our χ^2 analysis does not provide a strong constraint on the source size, we must adopt our original assumption that the CH₃OH and CH₃CHO source sizes are the same. In the shocks of L1157 the similar spatial distribution ($\sim 3''$ scales) of both species does suggest CH₃OH and CH₃CHO are coming from the same gas (Codella et al. 2020). Similarly, in Nagy et al. (2019) lower ($\sim 30''$) resolution CH₃OH and CH₃CHO maps of L1521E show overlap. If we assume an error of 20% in source size (see left panel Figure 9) we find a range of column densities for CH₃CHO, $N_{\text{tot}} = 2.3 - 3.8 \times 10^{12} \text{ cm}^{-2}$, which is still within the errors determined from our least squares fit to our rotation diagram (Table 3).

4 DISCUSSION

4.1 Abundance Comparison

We compare COM abundances to better understand how L1521E relates to other sites of low-mass star formation (Figure 12). Since CH₃OH is typically the most abundant COM, we find it interesting to investigate the abundance ratios of COMs w.r.t. CH₃OH, as well w.r.t. H₂. Overall, molecular abundances (w.r.t. H₂) increase between the prestellar and protostellar phase, yet the trend disappears when normalized by methanol.

The total COM abundances summed over all symmetry species are plotted in Figure 12 for fair comparison with literature values, i.e., in the case for CH₃CHO a total column density of the A + E states is calculated, not just the A state as quoted in Table 3. Two values for each COM abundance value derived for L1521E are also plotted, one if $f_v = 1$ was assumed (filled symbols) and one where the source size has been corrected using the assumption of the same spatial distribution as CH₃OH (open symbols).

Ordered roughly in an increasing evolutionary sequence, the molecular abundance w.r.t. H₂ of the starless and prestellar cores

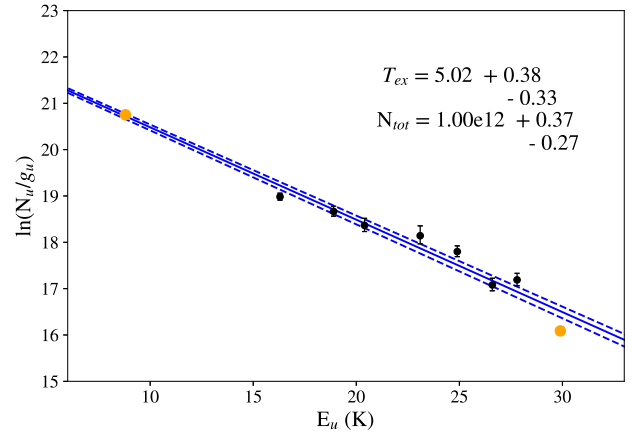


Figure 10. Rotation diagram for CH₂CHCN constructed from seven detected transitions (in black) and two non-detections that we use as 3σ upper limits (in orange). As in Figure 9, instead of errors based on solely the maximum and minimum fit from observed intensity uncertainties (the dashed lines), a least squares analysis is done to find more realistic errors to our linear fit.

tends to increase from left to right, and then drops off after L1689B, in Figure 12. Most comparable to less-evolved L1521E are the ‘typical’ starless cores in L1495/B218 as described in Scibelli & Shirley (2020), which range in abundance $X(\text{CH}_3\text{CHO}/\text{H}_2) = 0.4 - 2.2 \times 10^{-10}$. For prestellar core L183, embedded in the Serpens cloud, the CH₃CHO abundance falls in between these L1521E/L1495/B218 observations, with $X(\text{CH}_3\text{CHO}/\text{H}_2) = 1.0 \times 10^{-10}$ (Lattanzi et al. 2020).

In the prestellar core L1689B, all COM abundances are higher than those found in L1521E, referenced from COM column density values reported in Bacmann et al. 2012 and Bacmann & Faure 2016 assuming a $N(\text{H}_2)$ value of $4 \times 10^{22} \text{ cm}^{-2}$ (Bacmann et al. 2002). L1689B (central density $> 10^6 \text{ cm}^{-3}$; Steinacker et al. (2016)) has been measured to have a relatively low beam-averaged CO depletion factor of $N(\text{H}_2)_{\text{S850}}/N(\text{H}_2)_{\text{C17O}} = 2$ at its center, while for well-studied L1544 the CO beam-averaged depletion factor is > 9 at the center (Lee et al. 2003). L183 in Serpens (central density $> 10^6 \text{ cm}^{-3}$) sits in the middle of these two cores, as it is more depleted than L1689B but not as much as L1544, with a beam-averaged CO depletion factor ~ 6 (Pagani et al. 2007). Figure 12 shows that the more highly evolved L1544 (central density $> 10^7 \text{ cm}^{-3}$; Caselli et al. (2019)) is deficient in CH₃CHO when compared to all other dense cores at its dust peak position with $X(\text{CH}_3\text{CHO}/\text{H}_2) = 0.22 \times 10^{-10}$. As speculated in Scibelli & Shirley (2020), more evolved cores tend to have lower $X(\text{CH}_3\text{CHO}/\text{H}_2)$ abundances due to the depletion of precursors to COMs and depletion of COMs in the centers of cores.

It could be, however, that environmental effects are causing the large variations between the sources, rather than evolutionary effects. L1521E, L1495/B218, and L1544 are all located within Taurus and have similar abundance values, i.e., $X(\text{CH}_3\text{CHO}/\text{H}_2)$ varies by at most a factor of 10. As for other COMs, L1544’s abundance of CH₃OCH₃ is a factor of ~ 3 lower than that of L1521E, with a value of $X(\text{CH}_3\text{OCH}_3/\text{H}_2) = 0.28 \times 10^{-10}$. Abundances of HCOOCH₃ and CH₂CHCN are also a factor of ~ 3 lower, at $X(\text{HCOOCH}_3/\text{H}_2) = 0.81 \pm 0.74 \times 10^{-10}$ and $X(\text{CH}_2\text{CHCN}/\text{H}_2) = 0.22 \times 10^{-10}$ (Jiménez-Serra et al. 2016). When we compare the Taurus group (L1521E/L1495/B218/L1544) to L1689B in Ophiuchus we find, for example, $X(\text{CH}_3\text{CHO}/\text{H}_2)$ is at most 20 times larger. Because L1689B resides in the Ophiuchus molecular cloud, it is

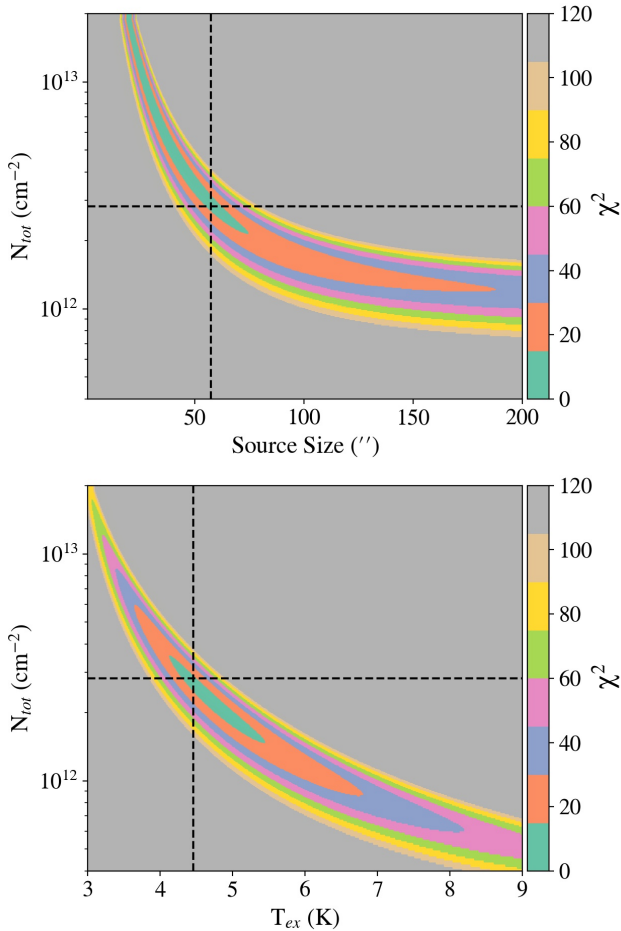


Figure 11. The χ^2 -value plots of CH_3CHO A column density versus (top) source size (") and (bottom) excitation temperature (K). The black dashed lines represent the calculated values found from our rotation diagram analysis, given a source size of $57''$, which crosses the minimized portion of the curve where $\chi^2 < 15$.

subject to different levels of exposure from the interstellar radiation field (ISRF). The radiation field is around two times the standard ISRF for L1689B (Steinacker et al. 2016), whereas for L1544 the strength of the UV field relative to the standard ISRF has only been slightly suppressed ($G_0 = 0.8$; Young et al. 2004). Still, these ISRF intensities (0.8 – 2.0) toward the dense, obscured cores at high extinction ($A_V > 10$ mag) might not be enough to affect local COM abundances. Differences in dense starless core COM abundances could be due to both their evolutionary stage as well as local environmental conditions. More observations of COMs in dense cores across many clouds are needed to say more.

We place in between the starless core and protostar category the dense cloud B5, which has higher COM abundance (w.r.t. H_2) values out of all the dense cores. Known as a methanol hot spot region, B5 is not classified as prestellar or protostellar (Taquet et al. 2017). Every starless and protostellar core plotted in Figure 12 has a well defined dust peak in submillimeter continuum emission, yet B5 does not. Thus, we stress that it's position in between starless and protostar does not imply evolution.

The enhancement of COMs in low-mass Class 0 and Class I protostars is illustrated in Figure 12, and is a trend that has been seen

before (e.g., López-Sepulcre et al. (2017)). In a process laid out recently by Coletta et al. (2020), who observed this same trend in a large sample of massive star-forming regions, molecular abundance will increase through thermal or shock induced desorption of COMs, first formed on ices.

There is also striking similarity (within a few orders of magnitude) between COM abundances w.r.t. CH_3OH , which highlights similar chemical evolution between different stages of low-mass star formation. When comparing abundance values w.r.t. CH_3OH across all evolutionary states, we find they vary roughly within an order of magnitude. Recent observations show distributions of COM abundances similarly enhanced in the cold component of the low-mass protostars B1-c, S68N and B1-bs, indicating that COMs could be inherited from the cold prestellar core phase (van Gelder et al. 2020). While some COMs could be inherited, the “warm-up” phase in protostars will increase COM formation efficiency (Garrod & Herbst 2006). Either CH_3OH is more abundant in protostellar sources or less abundant in prestellar cores when compared to other COMs (see section 4.2 for more on formation mechanisms).

Differences in individual protostar COM abundances are due to different physical conditions, since these systems are very dynamic and various heating processes from the accreting protostar, shocks, etc. can affect the local chemical environments. Figure 12 shows that the L1157B0b shock has the highest $X(\text{CH}_3\text{CHO}/\text{H}_2)$ abundance value (Codella et al. 2020). Additionally, inhomogeneity in analysis techniques can introduce bias when comparing values in the literature.

The recent comet measurements plotted in Figure 12 (with individual values for Hale-Bopp and Lovejoy) include average ranges for all Oort Cloud Comets (OCC) and as well as all Jupiter Family Comets (JFC) that were reported in Table 1 & 2 in Biver & Bockelée-Morvan (2019). One particular JFC comet, 67P/Churyumov-Gerasimenko (67P/C-G), is plotted separately and has been studied thoroughly by in situ measurements from the Rosetta mission (Schuhmann et al. 2019; Rubin et al. 2019). Similarly to protostars, comet abundances w.r.t. CH_3OH are comparable (order of magnitude) as those measured in the plotted cold cores (Figure 12), suggesting they contain preserved material from pre-solar system material.

Overall, it is evident that similarities in abundance throughout these stages of low-mass star formation implies that the solid-state processes are already enriching the complex organic inventory during the starless and prestellar core phase. Larger sample sets of sources (increased number of cores targeted) as well as COMs (a search for > a few COMs) are needed to say much more about the link between cold phase and warm phase chemistry.

4.2 Formation Mechanisms

Reactive desorption is thought to be one of the important mechanisms needed during the formation of COMs in cold cores. Vasyunin et al. (2017) models COM distribution in well-evolved L1544 with reactive desorption of radicals followed by the rapid gas-phase formation of COMs. The results of their models show that COM species peak in abundance on timescales of $2 \times 10^4 - 10^5$ years and at radii of 0.1 – 0.3 pc, consistent with the position of the CO freezeout radius in L1544 (see Figures 7 and 8 of Vasyunin et al. (2017)). At this position, the abundance of the “surface” CO ice, defined as the top four monolayers in their models, is at its peak.

The density of L1544 at these radii is very near the central density of L1521E at $3 \times 10^5 \text{ cm}^{-3}$. Radiative transfer models of C^{18}O 1-0 and 2-1 are consistent with a factor of a few depletion of CO in the center of L1521E (Ford & Shirley 2011). So, if CO were depleted

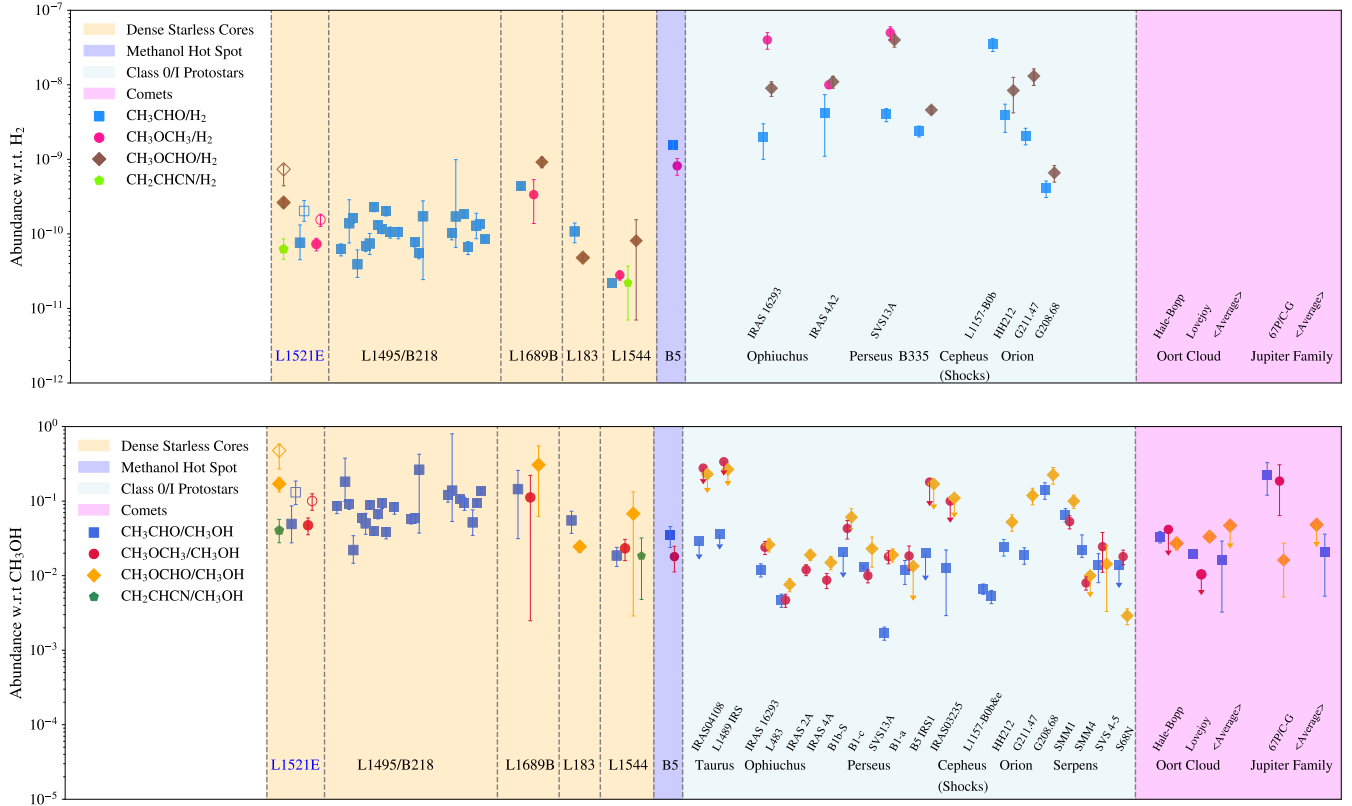


Figure 12. Comparison of COM abundances at various stages of low-mass star formation, including prestellar cores, hot cores and comets. Values for starless cores in L1495/B218 from [Scibelli & Shirley 2020](#), L183 from [Lattanzi et al. 2020](#), L1689B from [Bacmann et al. 2012](#), L1544 from [Jiménez-Serra et al. 2016](#), and for B5 from [Taquet et al. 2017](#). Note that for L1521E the open symbols represent values where source size was taken into account versus the filled symbols which represent values when $f_v = 1$ is assumed. Class 0/I protostars arranged (roughly) by cloud they reside in and/or distance (i.e., L483 has been associated with Serpens in the past but recent GAIA data places it at more like 200–250 pc). Protostar references: B1-c, B1-bs and S68N: ALMA band 3 values from [van Gelder et al. 2020](#); IRAS2A, IRAS4A: [Taquet et al. 2015](#); [López-Sepulcre et al. 2017](#); IRAS 16293-2422: [Jaber et al. 2014](#); [Jørgensen et al. 2018](#); SVS313A: [Bianchi et al. 2019](#); IRAS03245, B1-a, B5 IRS 1, SVS 4-5, IRAS 04108, L1489 IRAS: [Graninger et al. 2016](#); [Bergner et al. 2017](#); SMM1, SMM4: [Öberg et al. 2011](#); [Taquet et al. 2015](#); L483: [Jacobsen et al. 2019](#); L1157-B0e & L1157-B0b: [Codella et al. 2020](#); B335: [Imai et al. 2016](#); HH212, G211.47, G208.68: [Lee et al. 2019](#); [Hsu et al. 2020](#). We also include comparisons of the long-range comets, Hale-Bop and Lovejoy ([Biver & Bockelée-Morvan 2019](#)), as well as Jupiter-family comet, 67P/Churyumov–Gerasimenko (67/C-G) ([Schuhmann et al. 2019](#); [Rubin et al. 2019](#)). Values for 67/C-G are from the mass spectroscopy instrument aboard European Space Agency’s Rosetta mission, therefore isomers are indistinguishable (i.e., for CH_3OCHO this includes methyl formate, acetic acid and glycolaldehyde). Upper limit $X(\text{HCOOCH}_3/\text{CH}_3\text{OH})$ values and range of $X(\text{CH}_3\text{CHO}/\text{CH}_3\text{OH})$ values for all Oort Cloud Comets (OCC) and Jupiter Family Comets (JFC) also from [Biver & Bockelée-Morvan 2019](#).

by a factor of two then 50% of the gas phase CO has already frozen out of the gas phase and formed ice. A small amount of CO freeze-out onto the surface layers can drive radical formation with reactive desorption. In L1521E, the CO depletion radius may essentially be unresolved by current observations and be only in the very central region of the prestellar core. It is in these conditions, according to the models of [Vasyunin et al. \(2017\)](#), that the CO surface ice is maximized in abundance and COMs are formed rapidly.

We applied the chemical model described in [Vasyunin et al. \(2017\)](#), with several minor updates described in [Nagy et al. \(2019\)](#), to L1521E, correcting for its more shallower density profile than for L1544. A constant temperature is set to 10 K for our models presented here, and a total gas to dust mass ratio of 150:1 is assumed, to match our dust observations. In this work, we test the ‘Minissale&Dulieu’ (MD) approach, which changes the reactive desorption efficiency based on ice surface composition as well as on thermodynamics and complexity of products of individual chemical reactions that occur on ice surface (detailed in [Minissale et al.](#)

(2016)). The results obtained with MD model are presented in Figure 13.

We find that the estimated chemical age of L1521E is indeed young, as COMs first peak $\sim 6.0 \times 10^4$ yrs, consistent with the CO depletion age of the core. Our model, however, continues to overestimate CH_3OH abundances by roughly two orders of magnitude, a problem seen before and described in [Vasyunin et al. \(2017\)](#). We find that the observed abundance for CH_3CHO is reproduced by this model within a factor of 2, but the abundances of CH_3OCH_3 , HCOOCH_3 and CH_2CHCN are underpredicted by factors of 20–160. These COM abundances are underestimated, suggesting that we are either missing a desorption mechanism, or the current description of the already considered mechanisms should be revised in the future.

The failure of the model to fit CH_3OCH_3 and HCOOCH_3 may be partially due to the specific structure of L1521E since it is not as dense as other cores studied, has a low degree of CO freeze-out, and has higher sulfur abundance. Because the density is lower in comparison to L1544, the abundance of H tends to be higher than it

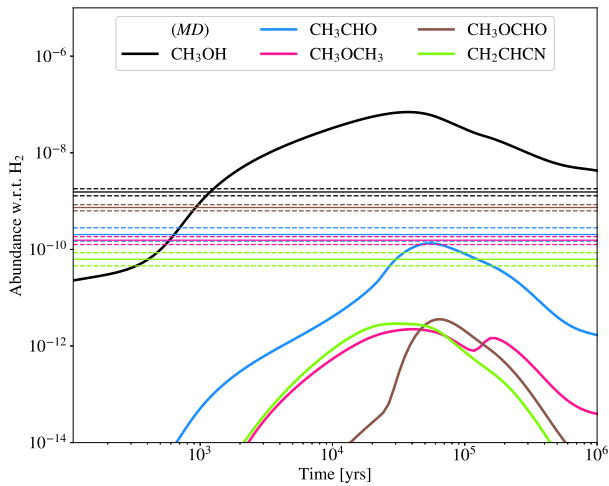


Figure 13. The chemical reactive desorption model used for L1521E is described as the ‘Minissale&Dulieu’ (MD) approach, where surface reactions dictate desorption efficiency, as described in Minissale et al. 2016 and Vasyunin et al. 2017. Our total (i.e., A + E states for CH₃CHO) calculated abundances, with uncertainties, are plotted as horizontal lines that match the color-scheme of the modeled curves.

is in dense gas. In our model, there is a reaction between atomic H and CH₃O to make CH₃ and OH. With more H, we find CH₃O, which is a precursor of CH₃OCH₃ and, indirectly, HCOOCH₃, is destroyed more efficiently leading to lower COM abundances in our model. Additionally, the model is sensitive to the elemental abundance of sulfur, affecting the abundance of atomic hydrogen on the grains through $gH + gHS \rightarrow gH_2S$ and $gH + H_2S \rightarrow gHS + gH_2$ reactions. L1521E has an elevated abundance of S in order to explain observed abundances of S-bearing species in Nagy et al. (2019). The peak abundance of some gas-phase COMs (e.g., CH₃OCH₃) increases when the elemental abundance of S is decreased.

As for CH₂CHCN, it is not reproduced by our model because there are no known efficient routes of its formation in the gas phase (see e.g. KIDA database; Wakelam et al. (2012)). When CH₂CHCN is formed on grains it does not desorb efficiently to the gas in M&D model, because this is a relatively polyatomic species, and energy released during the formation of CH₂CHCN is redistributed between many degrees of freedom in the molecule making the reactive desorption unlikely.

The high COM abundances in the low density starless core L1521E reveals the importance of alternative formation mechanisms, like non-diffusive chemistry. The non-diffusive chemical models, tailored for L1544, from Jin & Garrod (2020), do show that 3-body surface reactions can enhance COMs in the gas-phase up to the levels we see in L1521E as well. In their time-dependent models, CH₃OCH₃ is under produced while HCOOCH₃ is over produced (see their Figure 2). However, once they optimize the three-body excited-formation efficiency (3-BEF), originally assumed to proceed with 100% efficiency, HCOOCH₃ can be matched to the data. Unlike in our chemical reactive desorption models, they do not have the problem of over producing CH₃OH.

These chemical models have many uncertainties (i.e. extrapolation of reaction rates to 10 K, etc.), and there has not been a complete study of the initial conditions or full parameters space (see Vasyunin et al. (2004, 2008); Wakelam et al. (2005, 2006, 2010)). Despite not completely understanding the formation of COMs, we can still propose a basic scenerio where the core reaches densities of $\sim 10^5 \text{ cm}^{-3}$

and CO freezeout rapidly increases, then COMs are formed rapidly assisted by the reactive desorption of radicals and CH₃OH in the ice surface layers. As the central density increases, the COMs also begin to freeze out of the gas phase. The CO depletion radius moves out in the core as does the region of peak COM formation. Thus, peak COM formation proceeds in a wave that moves outward with time following the CO depletion radius as it propagates through the envelope. When the protostar forms, then the COMs that have frozen out in the densest regions of the core are released from the ices back into the gas phase from the inside outward.

How can we further test which physical mechanism is responsible for the formation of COMs in cold cores? CH₃OCH₃ is an interesting molecule to try and explain in cold environments, due to our current understanding of grain-surface radical chemistry. As demonstrated in Taquet et al. (2016) and Skouteris et al. (2019), the rate coefficients for the formation process of CH₃OCH₃ by purely gas-phase, ion-molecule routes are not efficient in cold objects like prestellar cores. The release of CH₃OCH₃ from the grains to the gas is problematic as laboratory experiments show that it would rather break the molecule (Minissale et al. 2016). One test is to look for the radical precursors that must be present in the gas phase to form the COMs.

Key reactions that are required for the formation of CH₃CHO in our model include the relative slow radiative association of CH₃ + HCO and the neutral-neutral reaction of CH + CH₃OH (Johnson et al. 2000). HCO and CH₃OH have been detected previously toward L1521E and are abundant ($> 10^{-10}$) in the gas phase (Bacmann & Faure 2016; Nagy et al. 2019). CH has its ground state, lambda doubled hyperfine transitions in its lowest energy ladder at 3.3 GHz, but no observations toward L1521E have been published. CH₃ is a planar molecule with no permanent electric dipole moment and cannot be easily observed in cold gas. Recent work has dismissed the formation of CH₃CHO from CH₃OH due to newly computed rate constants, instead favoring a formation route that starts from ethanol and the OH radical (Vazart et al. 2020), further motivating an investigation into alternative COM formation schemes.

An important reaction for the formation of CH₃OCH₃ appears to be the radiative association of CH₃O + CH₃ (i.e., Vasyunin & Herbst (2013); Balucani et al. (2015)). The CH₃O radical was not detected towards L1521E, constraining column density $N < 2.0 \times 10^{11}$ and $X(\text{CH}_3\text{O}/\text{HCO}) < 0.10$ (Bacmann & Faure 2016). For HCOOCH₃, which exhibits very similar radial and temporal behavior as CH₃OCH₃ in the models (Figure 13), a key chemical species is the hydroxyl radical, OH, which has been shown experimentally to react with CH₃OH to form key radical CH₃O. Our models here, and historically (e.g., Vasyunin & Herbst (2013)), have underestimated abundances of HCOOCH₃. However, recent studies have shown that HCOOCH₃ abundances can be increased by the addition of cosmic ray driven reactions (Shingledecker et al. 2018) and, as previously mentioned, through the non-diffusive surface chemistry (Jin & Garrod 2020).

From comparison of Figure 12 and Figure 13, one can conclude that “viable” scenarios of formation of COMs in star-forming regions must fulfill two constraints. First, models based on such scenarios must be able to reproduce observed fractional abundances of COMs w.r.t. hydrogen. Second, gas-phase abundance ratios between COMs and CH₃OH must be reproduced. The universality of COMs-to-methanol gas-phase abundance ratios revealed in Figure 12, supported by the fact that unlike H₂, abundance of CH₃OH can be derived directly in a consistent way with abundances of COMs, suggests very high importance of the second constraint. Our model, as described by Vasyunin et al. (2017), does not fulfill these constraints for L1521E. Thus, the gas-phase scenario of cold COM formation

is not sufficient in some cases. These results suggest that COMs observed in cold gas formed not only in gas-phase reactions, but also on surfaces of interstellar grains. Currently very little is known about exact mechanisms of transport of COMs possibly formed on cold grains ($T \sim 10\text{K}$) to the gas phase.

The detection of a rich COM chemistry in young cold core L1521E presents an interesting challenge for future modeling efforts, requiring some type of unified approach combining cosmic ray chemistry, reactive desorption and non-diffusive surface reactions.

5 CONCLUSIONS

Observations of COMs in the young starless core, L1521E, sheds light on the initial chemical conditions at one of the earliest stages of star formation. From our molecular line survey we find;

(i) The first detections of CH_3OCH_3 , HCOOCH_3 and CH_2CHCN in L1521E. Abundance ranges for each of these species are provided; i.e., $X(\text{CH}_3\text{OCH}_3/\text{H}_2) = 0.82 - 1.16 \times 10^{-10}$, $X(\text{HCOOCH}_3/\text{H}_2) = 2.14 - 3.42 \times 10^{-10}$, and $X(\text{CH}_2\text{CHCN}/\text{H}_2) = 0.31 - 1.17 \times 10^{-10}$.

(ii) A strong constraint on column density and T_{ex} (used to calculate abundances for the other oxygen-bearing COMs) of CH_3CHO from a rotation diagram analysis of five A-state transitions, gives an abundance range $X(\text{CH}_3\text{CHO}/\text{H}_2) = 1.24 - 2.53 \times 10^{-10}$.

(iii) Without taking into account source size when calculating column densities (i.e., assuming a filling fraction of 1), factors of a few in uncertainty arise. Thus, we stress the importance of high resolution maps of COMs in upcoming surveys.

(iv) The connection between L1521E, other starless and prestellar cores, low-mass hot cores and comets suggest that some COMs are seeded early on in the star formation process.

(v) The modeled COM formation mechanisms suggest that radical desorption plus gas-phase chemistry alone is not enough to account for the formation of COMs in the cold, dense environments native to prestellar cores.

(vi) We suggest that the ratio of gas-phase abundances of COMs to the abundance of methanol is an important constraint for scenarios of formation of complex organic species in star-forming regions.

ACKNOWLEDGMENTS

We thank our referee, Victor Rivilla, for their insightful comments and for improving the quality of this manuscript. We also thank Paola Caselli, Claudio Codella, Miwha Jin and Rob Garrod for their valuable conversations and insights that improved this paper. We are thankful that we have the opportunity to conduct astronomical research on Iolkam Du'ag (Kitt Peak) in Arizona and we recognize and acknowledge the very significant cultural role and reverence that these sites have to the Tohono O'odham Nation. We sincerely thank the operators of the Arizona Radio Observatory (Michael Begam, Kevin Bays, Clayton Kyle, and Robert Thompson) for their assistance with the observations. The 12 m Telescope is operated by the Arizona Radio Observatory (ARO), Steward Observatory, University of Arizona, with funding from the State of Arizona, NSF MRI Grant AST-1531366 (PI Ziurys), NSF MSIP grant SV5-85009/AST-1440254 (PI Marrone), NSF CAREER grant AST-1653228 (PI Marrone), and a PIRE grant OISE-1743747 (PI Psaltis). Yancy Shirley and Samantha Scibelli were partially supported by NSF Grant AST-1410190 (PI Shirley). Samantha Scibelli is supported by National Science Foundation Graduate Research Fellowship (NSF GRF) Grant DGE-1143953. Anton Vasyunin is supported by the Russian Ministry

of Science and Higher Education via the State Assignment Project FEUZ-2020-0038.

SOFTWARE

Astropy (*Astropy Collaboration et al. (2013), Astropy Collaboration et al. (2018)*), *NumPy* (*Harris et al. 2020*), *SciPy* (*Virtanen et al. 2020*), *Matplotlib* (*Hunter 2007*), *GILDAS CLASS* (*Pety (2005), Gildas Team (2013)*)

DATA AVAILABILITY

The data underlying this article will be shared on reasonable request to the corresponding author.

REFERENCES

- Aikawa Y., Wakelam V., Garrod R. T., Herbst E., 2008, *ApJ*, **674**, 984
 André P., Di Francesco J., Ward-Thompson D., Inutsuka S. I., Pudritz R. E., Pineda J. E., 2014, in Beuther H., Klessen R. S., Dullemond C. P., Henning T., eds, *Protostars and Planets VI*. p. 27 ([arXiv:1312.6232](https://arxiv.org/abs/1312.6232)), [doi:10.2458/azu_uapress_9780816531240-ch002](https://doi.org/10.2458/azu_uapress_9780816531240-ch002)
 Astropy Collaboration et al., 2013, *A&A*, **558**, A33
 Astropy Collaboration et al., 2018, *AJ*, **156**, 123
 Bacmann A., Faure A., 2016, *A&A*, **587**, A130
 Bacmann A., Lefloch B., Ceccarelli C., Castets A., Steinacker J., Loinard L., 2002, *A&A*, **389**, L6
 Bacmann A., Taquet V., Faure A., Kahane C., Ceccarelli C., 2012, *A&A*, **541**, L12
 Balucani N., Ceccarelli C., Taquet V., 2015, *MNRAS*, **449**, L16
 Beltrán M. T., Codella C., Viti S., Neri R., Cesaroni R., 2009, *ApJ*, **690**, L93
 Benson P. J., Myers P. C., 1989, *ApJS*, **71**, 89
 Bergin E. A., Tafalla M., 2007, *ARA&A*, **45**, 339
 Bergner J. B., Öberg K. I., Garrod R. T., Graninger D. M., 2017, *ApJ*, **841**, 120
 Bertoldi F., McKee C. F., 1992, *ApJ*, **395**, 140
 Bianchi E., et al., 2019, *MNRAS*, **483**, 1850
 Biver N., Bockelée-Morvan D., 2019, *ACS Earth and Space Chemistry*, **3**, 1550
 Butler R. A. H., De Lucia F. C., Petkie D. T., Møllendal H., Horn A., Herbst E., 2001, *ApJS*, **134**, 319
 Butscher T., Duvernay F., Theule P., Danger G., Carissan Y., Hagebaum-Reignier D., Chiavassa T., 2015, *MNRAS*, **453**, 1587
 Caselli P., et al., 2019, *ApJ*, **874**, 89
 Chen H. H.-H., et al., 2019, *ApJ*, **877**, 93
 Chuang K. J., Fedoseev G., Qasim D., Ioppolo S., van Dishoeck E. F., Linnartz H., 2017, *MNRAS*, **467**, 2552
 Codella C., et al., 2020, *A&A*, **635**, A17
 Coletta A., Fontani F., Rivilla V. M., Mininni C., Colzi L., Sánchez-Monge Á., Beltrán M. T., 2020, *A&A*, **641**, A54
 Costain C. C., Stoicheff B. P., 1959, *J. Chem. Phys.*, **30**, 777
 Endres C. P., Schlemmer S., Schilke P., Stutzki J., Müller H. S. P., 2016, *Journal of Molecular Spectroscopy*, **327**, 95
 Ford A. B., Shirley Y. L., 2011, *ApJ*, **728**, 144
 Fuller G. A., Myers P. C., 1992, *ApJ*, **384**, 523
 Garrod R. T., Herbst E., 2006, *A&A*, **457**, 927
 Gildas Team 2013, *GILDAS: Grenoble Image and Line Data Analysis Software* (ascl:1305.010)
 Gilmore W., Morris M., Johnson D. R., Lovas F. J., Zuckerman B., Turner B. E., Palmer P., 1976, *ApJ*, **204**, 43
 Graninger D. M., Wilkins O. H., Öberg K. I., 2016, *ApJ*, **819**, 140
 Harris C. R., et al., 2020, *arXiv e-prints*, [p. arXiv:2006.10256](https://arxiv.org/abs/2006.10256)
 Herbst E., van Dishoeck E. F., 2009, *ARA&A*, **47**, 427
 Hirota T., Ikeda M., Yamamoto S., 2001, *ApJ*, **547**, 814

- Hollis J. M., Lovas F. J., Jewell P. R., 2000, *ApJ*, 540, L107
- Hsu S.-Y., et al., 2020, *ApJ*, 898, 107
- Hunter J. D., 2007, *Computing in Science and Engineering*, 9, 90
- Ilyushin V., Kryvda A., Alekseev E., 2009, *Journal of Molecular Spectroscopy*, 255, 32
- Imai M., et al., 2016, *ApJ*, 830, L37
- Jaber A. A., Ceccarelli C., Kahane C., Caux E., 2014, *ApJ*, 791, 29
- Jacobsen S. K., Jørgensen J. K., Di Francesco J., Evans N. J., Choi M., Lee J.-E., 2019, *A&A*, 629, A29
- Jiménez-Serra I., et al., 2016, *ApJ*, 830, L6
- Jiménez-Serra I., et al., 2020, *Astrobiology*, 20, 1048
- Jin M., Garrod R. T., 2020, *ApJS*, 249, 26
- Johnson D. G., Blitz M. A., Seakins P. W., 2000, *Physical Chemistry Chemical Physics (Incorporating Faraday Transactions)*, 2, 2549
- Jørgensen J. K., et al., 2018, *A&A*, 620, A170
- Jørgensen J. K., Belloche A., Garrod R. T., 2020, *ARA&A*, 58, 727
- Kirk J. M., Ward-Thompson D., André P., 2005, *MNRAS*, 360, 1506
- Kirk H., Johnstone D., Tafalla M., 2007, *ApJ*, 668, 1042
- Kleiner I., Lovas F. J., Godefroid M., 1996, *Journal of Physical and Chemical Reference Data*, 25, 1113
- Lai J. C. Y., et al., 2017, *AJ*, 154, 206
- Lattanzi V., Bizzocchi L., Vasyunin A. I., Harju J., Giuliano B. M., Vastel C., Caselli P., 2020, *A&A*, 633, A118
- Launhardt R., et al., 2013, *A&A*, 551, A98
- Lee J.-E., Evans Neal J. I., Shirley Y. L., Tatematsu K., 2003, *ApJ*, 583, 789
- Lee C.-F., Codella C., Li Z.-Y., Liu S.-Y., 2019, *ApJ*, 876, 63
- Lippok N., et al., 2013, *A&A*, 560, A41
- López-Sepulcre A., et al., 2017, *A&A*, 606, A121
- Makiwa G., Naylor D. A., van der Wiel M. H. D., Ward-Thompson D., Kirk J. M., Eyres S., Abergel A., Köhler M., 2016, *MNRAS*, 458, 2150
- Mangum J. G., Shirley Y. L., 2015, *PASP*, 127, 266
- Marstokk K. M., Møllendal H., 1970, *Journal of Molecular Structure*, 5, 205
- Marstokk K. M., Møllendal H., 1973, *Journal of Molecular Structure*, 16, 259
- Minissale M., Dulieu F., Cazaux S., Hocuk S., 2016, *A&A*, 585, A24
- Müller H. S. P., Thorwirth S., Roth D. A., Winnewisser G., 2001, *A&A*, 370, L49
- Müller H. S. P., Schlöder F., Stutzki J., Winnewisser G., 2005, *Journal of Molecular Structure*, 742, 215
- Nagy Z., Spezzano S., Caselli P., Vasyunin A., Tafalla M., Bizzocchi L., Prudeniano D., Redaelli E., 2019, *A&A*, 630, A136
- Neustock W., Guarnieri A., Demaison J., Włodarczak G., 1990, *Zeitschrift Naturforschung Teil A*, 45, 702
- Öberg K. I., Bottinelli S., Jørgensen J. K., van Dishoeck E. F., 2010, *ApJ*, 716, 825
- Öberg K. I., van der Marel N., Kristensen L. E., van Dishoeck E. F., 2011, *ApJ*, 740, 14
- Ossenkopf V., Henning T., 1994, *A&A*, 291, 943
- Pagani L., Bacmann A., Cabrit S., Vastel C., 2007, *A&A*, 467, 179
- Pattle K., et al., 2015, *MNRAS*, 450, 1094
- Pety J., 2005, in Casoli F., Contini T., Hameury J. M., Pagani L., eds, SF2A-2005: Semaine de l'Astrophysique Française. p. 721
- Pickett H. M., Poynter R. L., Cohen E. A., Delitsky M. L., Pearson J. C., Müller H. S. P., 1998, *J. Quant. Spectrosc. Radiative Transfer*, 60, 883
- Redman M. P., Rawlings J. M. C., Nutter D. J., Ward-Thompson D., Williams D. A., 2002, *MNRAS*, 337, L17
- Rivilla V. M., Beltrán M. T., Vasyunin A., Caselli P., Viti S., Fontani F., Cesaroni R., 2019, *MNRAS*, 483, 806
- Rubin M., et al., 2019, in AGU Fall Meeting Abstracts. pp P43C–3489
- Schuhmann M., et al., 2019, *ACS Earth and Space Chemistry*, 3, 1854
- Scibelli S., Shirley Y., 2020, *ApJ*, 891, 73
- Seo Y. M., et al., 2015, *ApJ*, 805, 185
- Seo Y. M., et al., 2019, *ApJ*, 871, 134
- Shingledecker C. N., Tennis J., Le Gal R., Herbst E., 2018, *ApJ*, 861, 20
- Shirley Y. L., Nordhaus M. K., Grcevich J. M., Evans Neal J. I., Rawlings J. M. C., Tatematsu K., 2005, *ApJ*, 632, 982
- Simons M. A. J., Lamberts T., Cuppen H. M., 2020, *A&A*, 634, A52
- Sipilä O., Harju J., Juvela M., 2011, *A&A*, 535, A49
- Skouteris D., Balucani N., Ceccarelli C., Faginas Lago N., Codella C., Falcinelli S., Rosi M., 2019, *MNRAS*, 482, 3567
- Standards U. S. N. B. o., Wacker P., 1969, Microwave Spectral Tables. No. v. 3 in Microwave Spectral Tables, U.S. Department of Commerce, National Bureau of Standards, <https://books.google.com/books?id=vbrvAAAAAAAJ>
- Steinacker J., Bacmann A., Henning T., Heigl S., 2016, *A&A*, 593, A6
- Suzuki H., Yamamoto S., Ohishi M., Kaifu N., Ishikawa S.-I., Hirahara Y., Takano S., 1992, *ApJ*, 392, 551
- Tafalla M., Santiago J., 2004, *A&A*, 414, L53
- Taquet V., López-Sepulcre A., Ceccarelli C., Neri R., Kahane C., Charnley S. B., 2015, *ApJ*, 804, 81
- Taquet V., Wirstrom E. S., Charnley S. B., 2016, *ApJ*, 821, 46
- Taquet V., Wirstrom E. S., Charnley S. B., Faure A., López-Sepulcre A., Persson C. M., 2017, *A&A*, 607, A20
- Vastel C., Ceccarelli C., Lefloch B., Bachiller R., 2014, *ApJ*, 795, L2
- Vasyunin A. I., Herbst E., 2013, *ApJ*, 769, 34
- Vasyunin A. I., Sobolev A. M., Wiebe D. S., Semenov D. A., 2004, *Astronomy Letters*, 30, 566
- Vasyunin A. I., Semenov D., Henning T., Wakelam V., Herbst E., Sobolev A. M., 2008, *ApJ*, 672, 629
- Vasyunin A. I., Caselli P., Dulieu F., Jiménez-Serra I., 2017, *ApJ*, 842, 33
- Vazart F., Ceccarelli C., Balucani N., Bianchi E., Skouteris D., 2020, *MNRAS*, 499, 5547
- Virtanen P., et al., 2020, *Nature Methods*, 17, 261
- Wakelam V., Selsis F., Herbst E., Caselli P., 2005, *A&A*, 444, 883
- Wakelam V., Herbst E., Selsis F., 2006, *A&A*, 451, 551
- Wakelam V., Herbst E., Le Bourlot J., Hersant F., Selsis F., Guilloteau S., 2010, *A&A*, 517, A21
- Wakelam V., et al., 2012, *ApJS*, 199, 21
- Watanabe N., Kouchi A., 2002, *ApJ*, 571, L173
- Young K. E., Lee J.-E., Evans Neal J. I., Goldsmith P. F., Doty S. D., 2004, *ApJ*, 614, 252
- di Francesco J., Evans N. J. I., Caselli P., Myers P. C., Shirley Y., Aikawa Y., Tafalla M., 2007, in Reipurth B., Jewitt D., Keil K., eds, Protostars and Planets V. p. 17 ([arXiv:astro-ph/0602379](https://arxiv.org/abs/astro-ph/0602379))
- van Gelder M. L., et al., 2020, *A&A*, 639, A87

This paper has been typeset from a $\text{\TeX}/\text{\LaTeX}$ file prepared by the author.